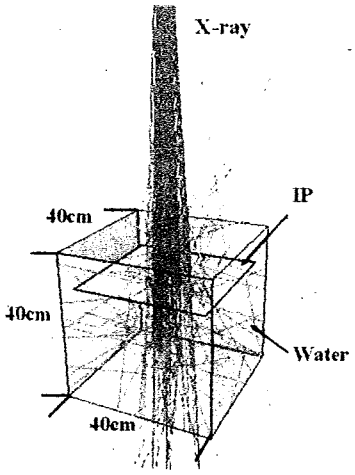

FIG. 3. Example showing the behavior of 100 photons in the water phantom.

corresponding data area on the IP, 100×100 pixels with each pixel being 0.1×0.1 mm^2, and which was compared with the one with ion chamber.

2. MC simulation

The geometrical setup is shown in Fig. 2. First, the PDD and OAR at 10 cm depth were calculated without anything placed in water phantom, where these calculated data were compared with the measured data from the ionization chamber. The voxel size used for the calculation of the water absorbed dose was $5\times5\times5$ mm^3. For the simulation with the IP, the IP was placed perpendicular to the beam axis at a depth of 10 cm, and the OAR was obtained by calculating the dose to the phosphor layer. The voxel size used for this calculation was 5 mm$\times$5 mm$\times$210 μm. Figure 3 is a schematic showing the result of the calculation.

B. Investigating the filter by MC simulation

This calculation also followed the above procedure. The size of filters used in the simulation was 35×35 cm^2, and the filters were set, as shown in Fig. 4, in three different configurations: above only, below only, and one on each side simultaneously. The material, thickness, and displacement of the filters were varied. The same simulation was repeated without the IP and filters, from which the OAR was obtained and used as a reference for comparison. From the simulation, the appropriate filter was identified as the one for which the calculation result was closest to the OAR data without the IP. The following formula was used to determine which data gave the closest comparison,

$$(\text{relative error})_r(\%) = \frac{(\text{OAR}_{\text{IP},r} - \text{OAR}_{W,r})}{\text{OAR}_{W,0}} \times 100,$$

where $\text{OAR}_{\text{IP},r}$ is OAR on the IP (the phosphor layer) at r millimeters from the central axis. $\text{OAR}_{W,r}$ is OAR with the IP and the filter in r millimeters from the central axis and likewise $\text{OAR}_{W,0}$ is the one in 0 mm from central axis. Unless stated, the value for the OAR is computed with the arithmetic average of relative errors locating from -60 to -100 mm from central axis at a 10 cm depth, where the errors obviously show up, with a 10×10 cm^2 field size and 100 cm SSD.

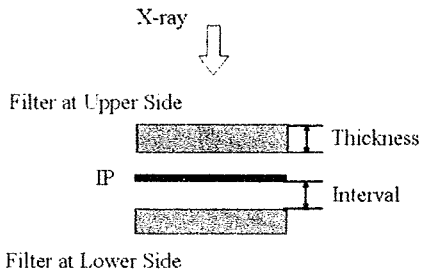

FIG. 4. Schematic diagram showing the location of double filters placed on both sides of the IP. The size of the filter was 35×35 cm^2. The material, thickness, and the distance between the IP and the filter were varied.

1. Material of the filters

The materials used in this evaluation are simple substances with atomic number (Z) from 4 to 82. Concerning the material data, the simulation was carried out in two ways, one simply using the density of every material,[22] the other setting the density to the one of lead, 11.35 g/cm^3, for all the materials in order to observe the Z dependency. The thickness was fixed to 2 mm and there was no gap between the filter and the IP.

2. Filter thickness

For this evaluation, only the lead filter was used. The filter thickness was varied from 0 to 15 mm and there was no gap between the filter and IP in the calculation.

3. Filters displacement

The lead filter was also used for this calculation. The distance between the IP and the filter (expressed by "Interval" in Fig. 4) was varied from 0 to 15 mm for two cases; filter thicknesses of 2 and 1 mm. We set water equivalent data in the interval.

III. RESULTS AND DISCUSSIONS

A. MC simulation parameter settings and evaluation

As reported by Olch,[11] the dependence of the pixel value from IP measurement on dose is given in Fig. 5, and this is expressed by a logarithmic relationship. The energy spectrum used in the simulation is shown in Fig. 6. For comparison, the results of the calculation and the measured PDD and OAR are shown in Fig. 7. As can be seen in Fig. 7(a), the calculated depth dose relationship is in good agreement with the measured data. From Fig. 7(b) we can find the average values of the relative error from -60 to -100 mm from the central axis with and without the IP. These are $20.7\pm2.6\%$ for the measurement and $20.5\pm3.0\%$ for the simulation, showing good agreement for the OAR. These results infer that the MC simulation settings used were realistic.

Downloaded 02 Feb 2010 to 133.11.102.2. Redistribution subject to AIP license or copyright; see http://rsi.aip.org/rsi/copyright.jsp

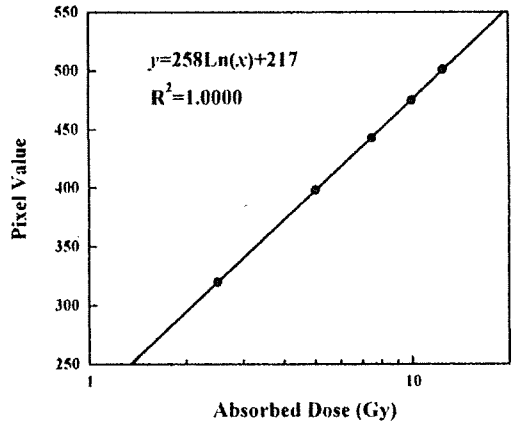

FIG. 5. Relationship between absorbed dose and pixel value along the central axis of a 10×10 cm^2 field in 10×10 mm^2.

B. Investigating the filter by MC simulation

The calculated OAR is shown in Fig. 8, which shows that, compared with the dose in water (dose with no IP in water), there is a $20.5\pm3.0\%$ difference in the average value of the relative error from -60 to -100 mm from central axis with the IP only, a $15.3\pm2.7\%$ difference for the IP with a 2 mm copper filter placed above it and a $9.8\pm2.2\%$ difference for the IP with a lead filter. It can be seen that the use of filters shifts the result closer to the dose in water with no IP.

First, we shall discuss the appropriate material to be used for the filter. A similar calculation to that shown in Fig. 8 was done for each material in order to determine the appropriate filter. The results are shown in Fig. 9. As the results show, placing a filter on each side of the IP produced a better effect than with a single filter on either side. In Fig. 9(a), compared to Ag(Z=47) and Nd(Z=60), Ba(Z=56) has a higher relative error based on t-tests ($P<0.001$). This is because Ba has a density of 3.5 g/cm^3 and thus, compared with Ag (density: 10.5 g/cm^3) and Nd (density: 6.9 g/cm^3), has a smaller ratio between density and Z. On the other hand, Fig. 9(b) shows the Z dependency only for filter materials (Z=4–82), from which we can see that the effect produced by the filter improves as Z increases, and, as the results indicate, using a high density filter material on both sides leads to a much better effect. Considering the results and the materials that are practical to use, we conclude that Pb would be the most appropriate filter material.

Our second discussion is with regard to the filter thickness. The MC simulation results are shown in Fig. 10, which

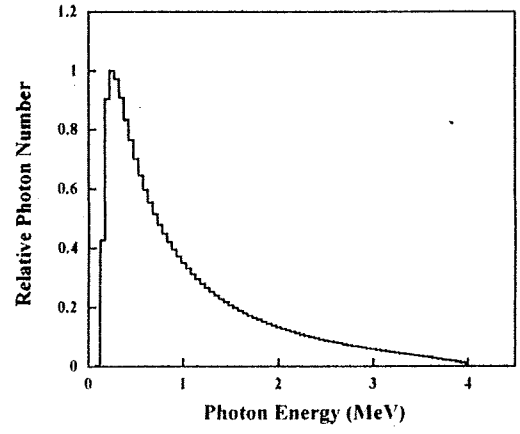

FIG. 6. Photon energy spectrum used in MC calculation.

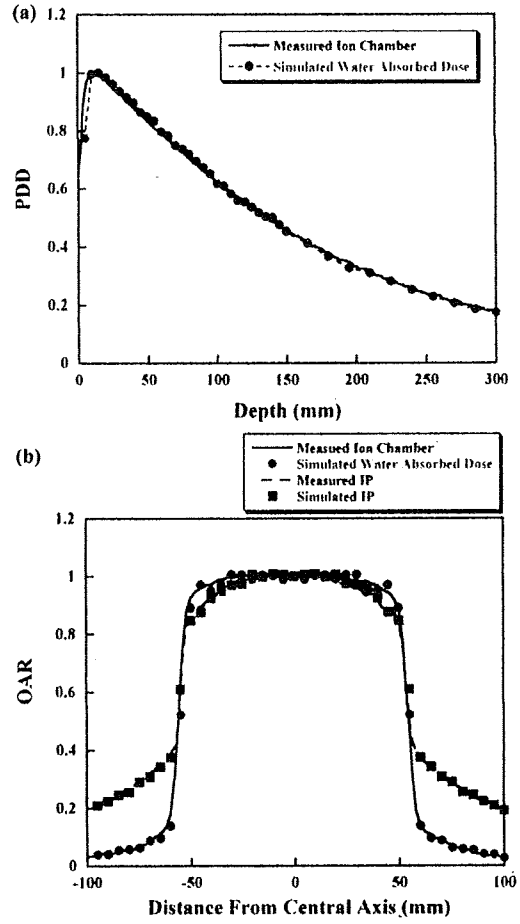

FIG. 7. Comparison of MC calculation with measurements. (a) PDD in beam axis. (b) OAR at 10 cm depth.

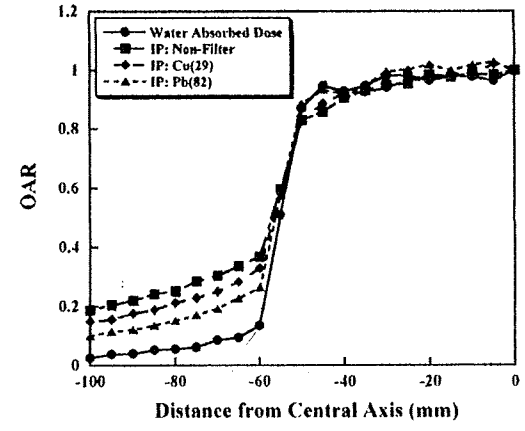

FIG. 8. Comparison of the OAR in water for nonfilter and 2 mm thick Cu and Pb filters where the filter is placed in contact with the IP.

Downloaded 02 Feb 2010 to 133.11.102.2. Redistribution subject to AIP license or copyright; see http://rsi.aip.org/rsi/copyright.jsp

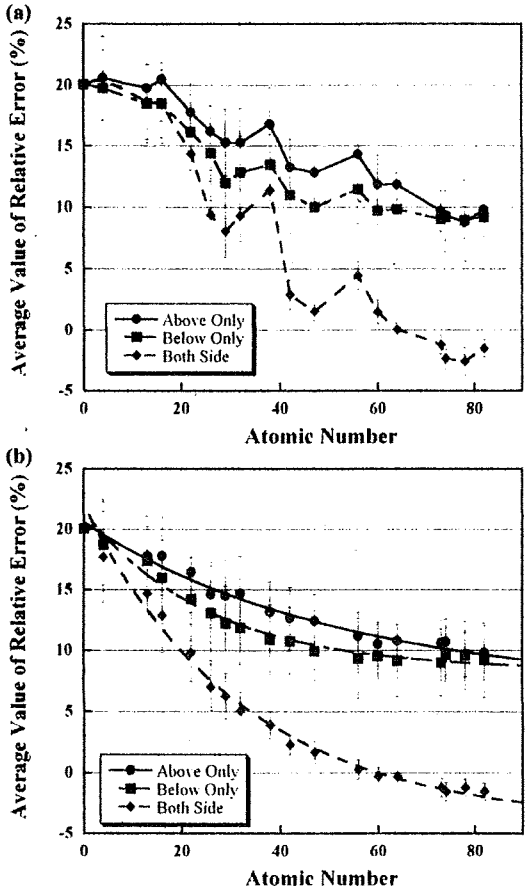

FIG. 9. Average value of relative error from −60 to −100 mm from the central axis for different filter materials. Atomic number 0 means that no filter is used. (a) Result using the density (g/cm^3) associated with each atomic number. (b) Similar to (a) but using a constant density value of 11.35 g/cm^3 for each atomic number material.

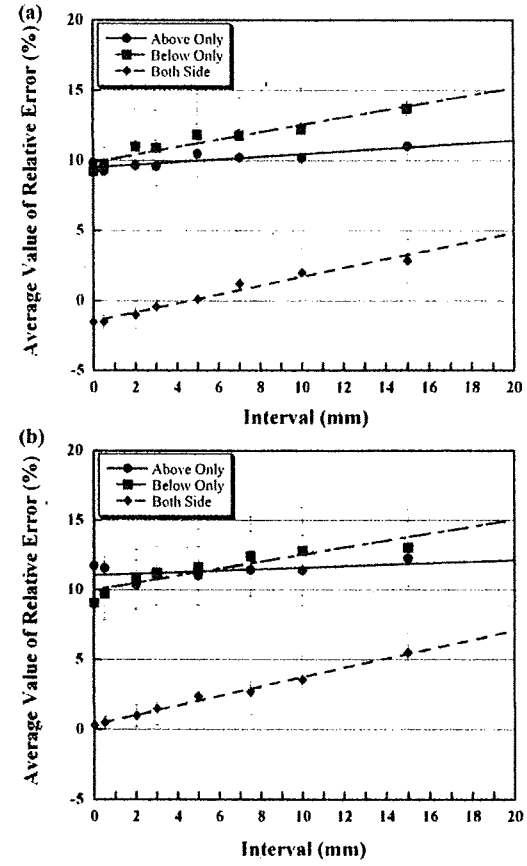

FIG. 11. Average value of relative error as a function of the distance between the filters and the IP (interval). Interval 0 means that these are in contact. (a) Average values of relative error using a 2 mm thick Pb filter. (b) Average values of relative error using a 1 mm thick Pb filter.

shows the relationship between the relative error and the thickness of the Pb filter from −60 to −100 mm from central axis. It can be seen that there is a general trend for the relative error to fall to a constant value as the filter thickness is increased. For the filter placed under the IP, this occurs for a thickness of 1 mm, and is due to the contribution of low energy photons scattered from the IP. According to the results, good agreement was found between the calculated OAR without an IP and when using 1 mm thick Pb filters on each side of the IP. If filters thicker than 1 mm are used, the effect becomes excessive. As shown in Fig. 10, the gradient of the relative error curve is steep at 1 mm, so that, when making the filter, care should be taken in the precision of the thickness; for example, if the filter were to be 0.75 or 1.5 mm in thickness, relative errors of $1.8 \pm 0.8\%$ or $-0.9 \pm 0.6\%$, respectively, would arise.

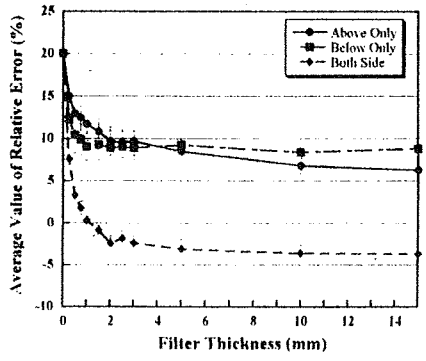

FIG. 10. Average value of relative error vs Pb filter thickness. Filter thickness 0 means no filter is used.

So far we have determined the most suitable material and the thickness of the filter. Finally, we discuss the position of the filter with respect to the IP. The relationship between the relative error and the distance of the Pb filter from the IP was calculated. Figure 11 represents the results for 2 mm thick Pb filters [Fig. 11(a)] as well as 1 mm thick filters [Fig. 11(b)]. There is no significant position dependent effect observed for the filter placed above the IP; whereas, for ones placed beneath or on both sides of the IP, the relative errors increase linearly as the distance between the IP and the filter increases. It is indicated that the filter effect tends to diminish. The scattered photons basically have a lower energy spectrum and scatter into a larger solid angle. In addition to this, since the IP includes high atomic number (Z) materials,

Downloaded 02 Feb 2010 to 133.11.102.2. Redistribution subject to AIP license or copyright; see http://rsi.aip.org/rsi/copyright.jsp

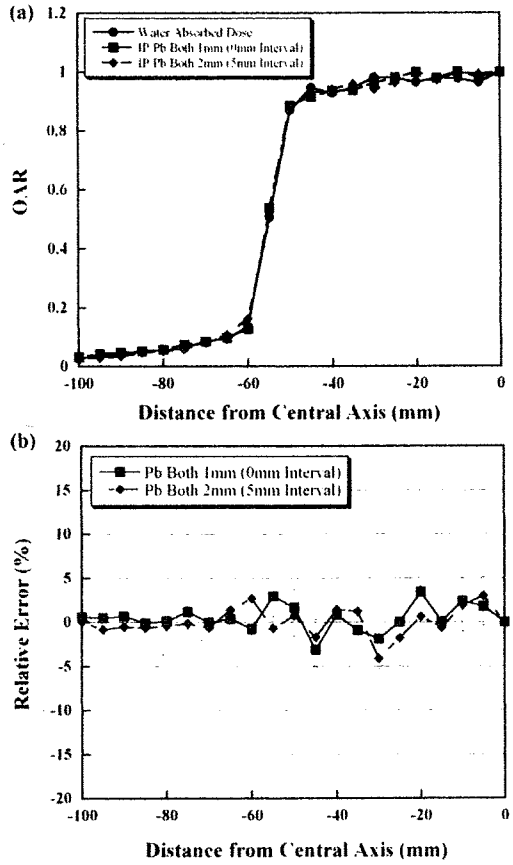

FIG. 12. (a) Comparison between the OAR calculated in water (no IP) and the OAR in water with an IP with 1 mm thick Pb filters and 2 mm thick Pb filters. (b) Relative error vs distance from the central axis.

such as Ba, the lower energy photons are attenuated much than higher ones. This is how the ratio of the energy given to IP by the backscattered photons from down stream of the IP is greater than that by photons scattered from upper stream of IP where water exist between the IP and the filter and the scatter is caused mainly by interaction with water. Therefore, the contribution to the IP of photons backscattered from under the IP is much larger than photons scattered from the upper side of the IP. This is the reason, if the interval is large, the filter position affects the relative errors. Essentially, the best options for position found from the results are with filters placed on each side of the IP, either with 2 mm Pb filters with a 5 mm interval or 1 mm Pb filters with a 0 mm interval (i.e., filters attached to both sides of the IP). Note that precision is also needed when placing the filters at the recommended distances. The OARs of the optimum filter positions and that without an IP (OAR in water) are shown in Fig. 12(a). In addition, the relative errors derived from the results in Fig. 12(a) are shown in Fig. 12(b), which showed that the relative errors of 1 mm Pb filters with a 0 mm interval and 2 mm Pb filters with a 5 mm interval distributed around 0% both in and out of the field. There was a good agreement with the result of the water absorbed dose. In detail, we calculated the root mean square of the relative error in terms of out-of-field (from −60 to −100 mm) and in-field (from

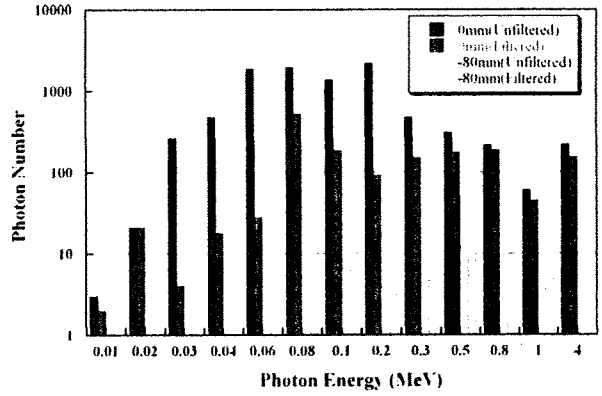

FIG. 13. Comparison of the energy spectra of photons (1×10^8 photons) interacting in the IP, on the beam axis and at −80 mm from the central axis for the cases with no filter and 1 mm thick Pb filters attached to each side of the IP.

0 to −50 mm). The results of 1 and 2 mm thick Pb filters were 2.0% and 2.0% in the field and 0.6% and 1.1% out of the field, respectively. Thus, this simulation study indicated that, by using two 1 mm thick Pb filters attached to each side of the IP or two 2 mm thick Pb filters placed 5 mm from each side of the IP, it is possible to obtain OAR curve with IP as accurate as the one based on the absorbed dose calculated only in water.

We also investigated the energy spectra in the IP with and without filters. We calculated the energy spectrum in each case from the MC analysis and the results are shown in Fig. 13. What the figure shows is that the number of photons in the low energy range (especially keV range), where there is an energy dependency on the IP, is reduced by the filter. Thus, the accuracy of the IP measurement is improved when the filter is used. The OAR measurement, in particular, can be done without concern about the energy dependency of the IP.

In study of Olch,[11] a 0.4 mm Pb filter was placed on both sides of an IP and a 6 MV photon OAR measurement was done. This is different from our study where 1 mm Pb filters were attached to both sides of the IP. What we have done in our study is completely different to his research with respect to using different IPs, energies, different procedures, and so on. To make a comparison with his study and also to develop a more reliable filter, a further more detailed study using more sophisticated calculation conditions would be needed. Additionally a certain distance of 5 mm from each side of the IP obtained in this study was suggested as one of parameters for using the Pb filters as simply as possible. This was the result that we tried to figure out some parameters as less as possible, by which it is expected that the quality assurance would be performed easily and quickly. However, it may also be important that the consideration of specific parameters suitable for each measurement condition would be needed to investigate the possibility of use of IP as a quality assurance tool with high accuracy.

[1] L. Stanton, Radiology **78**, 445 (1962).
[2] J. F. Williamson, F. M. Khan, and S. C. Sharma, Med. Phys. **8**, 94 (1981).
[3] C. W. Cheng and I. J. Das, Med. Phys. **23**, 1225 (1996).

Downloaded 02 Feb 2010 to 133.11.102.2. Redistribution subject to AIP license or copyright; see http://rsi.aip.org/rsi/copyright.jsp

[4]P. Cadman, Med. Phys. **25**, 1435 (1998).
[5]M. D. R. Thomas and A. P. Warrington, Phys. Med. Biol. **51**, 1439 (2006).
[6]M. Fuss, E. Sturtewagen, C. D. Wagter, and D. Georg, Phys. Med. Biol. **52**, 4211 (2007).
[7]L. J. van Battum, D. Hoffmans, H. Piersma, and S. Heukelom, Med. Phys. **35**, 704 (2008).
[8]M. Sonoda, M. Takano, J. Miyahara, and H. Kato, Radiology **148**, 833 (1983).
[9]J. A. Rowlands, Phys. Med. Biol. **47**, R123 (2002).
[10]S. M. Kengyelics, A. G. Davies, and A. R. Cowen, Med. Phys. **25**, 2163 (1998).
[11]A. J. Olch, Med. Phys. **32**, 2987 (2005).
[12]M. Homma, K. Tabushi, Y. Obata, T. Tamiya, S. Koyama, and T. Ishigaki, Jpn. J. Med. Phys. **22**, 118 (2002).
[13]H. H. Li, A. L. Gonzalez, H. Ji, and M. Duggan, Med. Phys. **34**, 103 (2007).
[14]S. E. Burch, K. J. Kearfott, J. H. Trueblood, W. C. Shiels, J. I. Yeo, and C. K. Wang, Med. Phys. **24**, 775 (1997).
[15]I. J. Yeo, C. K. Wang, and S. E. Burch, Med. Phys. **24**, 1943 (1997).
[16]S. G. Ju, Y. C. Ahn, S. J. Huh, and I. J. Yeo, Med. Phys. **29**, 351 (2002).
[17]S. Agostinelli, J. Allison, K. Amako, J. Apostolakis, H. Araujo, P. Arce, M. Asai, D. Axen, S. Banerjee, G. Barrabd, F. Behner, *et al.*, Nucl. Instrum. Methods Phys. Res. A **506**, 250 (2003).
[18]L. I. Schiff, Phys. Rev. **83**, 252 (1951).
[19]G. E. Desobry and A. L. Boyer, Med. Phys. **18**, 497 (1991).
[20]C. R. Baker, B. Ama'ee, and N. M. Spyrou, Phys. Med. Biol. **40**, 529 (1995).
[21]M. Partridge, Phys. Med. Biol. **45**, N115 (2000).
[22]S. M. Seltzer and J. H. Hubblell, *Photon Attenuation Coefficient Data Book* (Japan Society of Radiological Technology, Kyoto, 1995).

Downloaded 02 Feb 2010 to 1.3.11.1xx. Redistribution subject to AIP license or copyright; see http://rsi.aip.org/rsi/copyright.jsp

THE JOURNAL OF
DERMATOLOGY

doi: 10.1111/j.1346-8138.2009.00729.x

Journal of Dermatology 2009; **36**: 663–665

LETTER TO THE EDITOR

Iatrogenic vulvar skin metastases after interstitial radiotherapy for recurrent cervical cancer

Dear Editor,

We report a case of a 68-year-old woman with iatrogenic vulva skin metastasis after interstitial radiotherapy (ISRT) was performed for recurrence in the vaginal stump of uterine cervical carcinoma. At age 65 years, she complained of atypical vaginal bleeding. The diagnosis was uterine cervical adenosquamous carcinoma with direct vaginal invasion. She received abdominal radical hysterectomy, bilateral salpingo-oophorectomy, pelvic lymphadenectomy, and para-aortic lymphadenectomy in our institution on 31 August 2006. The pathological stage was T2aN0M0. Postoperative adjuvant whole pelvic radiotherapy using four-portal box fields (50.4 Gy in 28 fractions) was performed because of deep invasion (>1/2) to the muscle layer from 21 September 2006.

On 14 August 2008, high-dose-rate ISRT was started using iridium-192 (36 Gy in six fractions twice a day for 3 successive days). A Martinez Universal Perineal Interstitial Template (MUPIT) utilizing eight metal needle applicators[1,2] with individual diameters of 1.5 mm and lengths of 160–200 mm for Micro-Selectron HDR (Chiyoda Technol, Tokyo, Japan) were used for the recurrence in the postoperative vaginal stump (Fig. 1). The external view is shown in Figure 1(a), the scout view of computed tomography in Figure 1(b), and the dose distribution in the machine for radiotherapy planning in Figure 1(c). On January 2009, multiple vulvar skin metastases were found (Fig. 2). The metastatic lesions approximated with the sites on the skin where the needle applicators had been inserted, and where she complained of pain. On 20 January 2009, a biopsy of the vulva skin was performed. The diagnosis was poorly differentiated carcinoma involving the vulva (Fig. 3a), and which was consistent with metastases from previously resected primary uterine cervical carcinoma (Fig. 3b).

Interstitial radiotherapy by MUPIT is a good choice to deliver high-dose radiation in recurrent gynecological malignancies after external beam radiotherapy where conventional brachytherapy application is not feasible and is likely to give optimal dose distribution. Furthermore, locoregional control obtained with ISRT is good and within the accepted range of complications.[3–5] This MUPIT template consists of a central large hole for placement of tandem and an array of small holes around this large hole for insertion of needles. The eight needles were inserted into the tumor and surrounding tissue and withdrawn on the final day. Uterine cervical carcinoma typically advances in a predictable fashion locally and through the lymphatic route. Lymphatic metastases usually occur first in the pelvic nodes and later in the para-aortic and/or supraclavicular nodes. In more advanced stages, the tumor cells spread hematogenously, representing lung or liver metastases. According to Sakurai *et al.*[6] in Gunma University, a total of 74 out of 256 patients (29%) between 1976 and 1994 had recurrence after definitive radiation therapy alone, and regarding first sites of recurrence, recurrent locoregional cancers were identified in 22 patients (30%), lymphogenous cancer in 22 patients (30%) and hematogenous in 19 patients (26%). Of the lymphogenous recurrences, eight (36%) developed in para-aortic nodes, 11 (50%) developed in supraclavicular nodes and three (14%) developed at both sites. Cervical cancer often spreads through direct local extension and through the lymphatics and skin. Also, cutaneous metastases from cervical cancer are very rare (i.e. <2%).[7–9] Therefore, it is considered that iatrogenic skin metastasis after ISRT occurred in this case through the same mechanism of intra- and extrahepatic disseminations of hepatocellular carcinoma after radiofrequency thermal

Correspondence: H. Yamashita, M.D., Ph.D., Department of Radiology, University of Tokyo Hospital, 7-3-1 Hongo, Bunnkyou-ku, Tokyo 113-8655, Japan. Email: yamashitah-rad@h.u-tokyo.ac.jp

© 2009 Japanese Dermatological Association

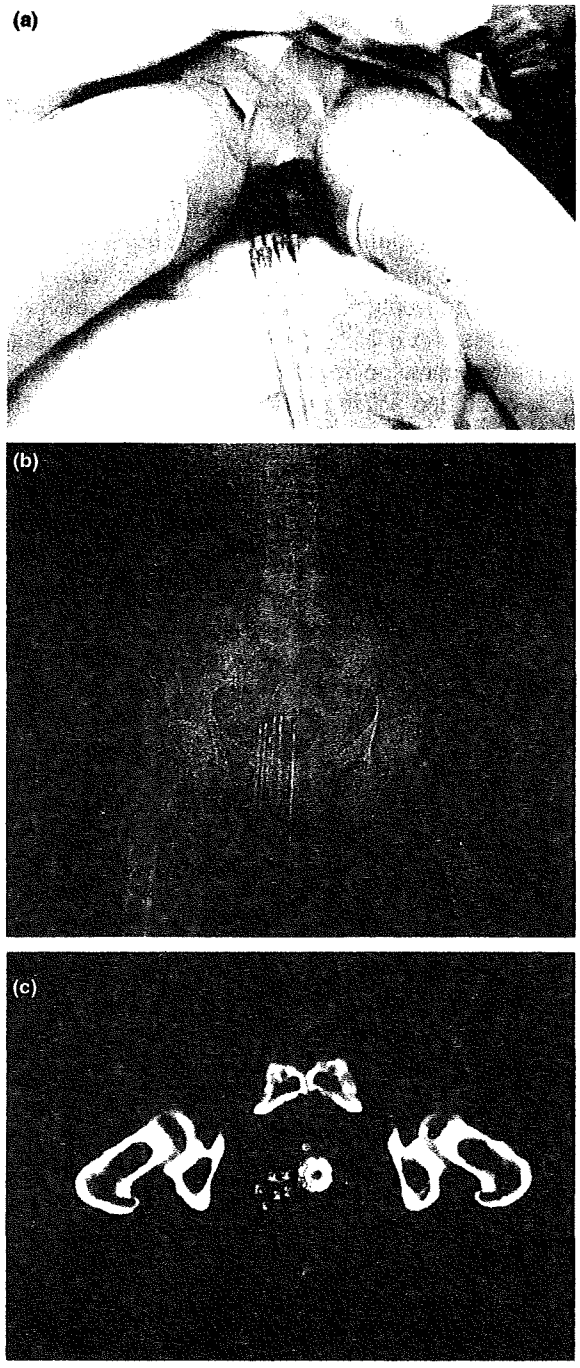

Figure 1. Interstitial radiotherapy with eight metal applicators. (a) External view; (b) scout view of computed tomography (CT); (c) dose distribution in the machine for radiotherapy planning.

Figure 2. Iatrogenic multiple vulvar skin metastases.

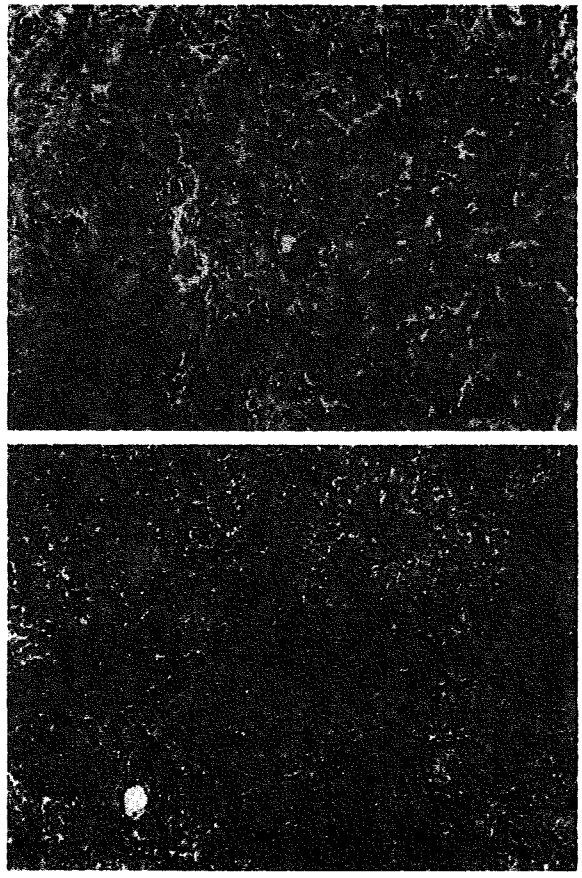

Figure 3. Hematoxylin–eosin staining. Poorly differentiated carcinoma involving (a) the vulva and (b) previously resected primary uterine cervical carcinoma (original magnifications ×100).

© 2009 Japanese Dermatological Association

ablation.[10] To our knowledge, iatrogenic skin metastasis after ISRT has not been previously reported.

Hideomi YAMASHITA,
Kae OKUMA, Keiichi NAKAGAWA
Departments of Radiology, University of Tokyo Hospital, Tokyo, Japan

REFERENCES

1 Nandwani PK, Vyas RK, Neema JP, Suryanarayan UK, Bhavsar DC, Jani KR. Retrospective analysis of role of interstitial brachytherapy using template (MUPIT) in locally advanced gynecological malignancies. *J Cancer Res Ther* 2007; **3**: 111–115.
2 Martinez A, Edmundson GK, Cox RS, Gunderson LL, Howes AE. Combination of external beam irradiation and multiple-site perineal applicator (MUPIT) for treatment of locally advanced or recurrent prostatic, anorectal, and gynecologic malignancies. *Int J Radiat Oncol Biol Phys* 1985; **11**: 391–398.
3 Gupta AK, Vicini FA, Frazier AJ *et al.* Iridium-192 transperineal interstitial brachytherapy for locally advanced or recurrent gynecological malignancies. *Int J Radiat Oncol Biol Phys* 1999; **43**: 1055–1060.
4 Agrawal PP, Singhal SS, Neema JP *et al.* The role of interstitial brachytherapy using template in locally advanced gynecological malignancies. *Gynecol Oncol* 2005; **99**: 169–175.
5 Itami J, Hara R, Kozuka T *et al.* Transperineal high-dose-rate interstitial radiation therapy in the management of gynecologic malignancies. *Strahlenther Onkol* 2003; **179**: 737–741.
6 Sakurai H, Mitsuhashi N, Takahashi M *et al.* Analysis of recurrence of squamous cell carcinoma of the uterine cervix after definitive radiation therapy alone: patterns of recurrence, latent periods, and prognosis. *Int J Radiat Oncol Biol Phys* 2001; **50**: 1136–1144.
7 Imachi M, Tsukamoto N, Kinoshita S, Nakano H. Skin metastasis from carcinoma of the uterine cervix. *Gynecol Oncol* 1993; **48**: 349–354.
8 Srivastava K, Singh S, Srivastava M, Srivastava AN. Incisional skin metastasis of a squamous cell cervical carcinoma 3.5 years after radical treatment – a case report. *Int J Gynecol Cancer* 2005; **15**: 1183–1186.
9 Behtash N, Ghaemmaghami F, Yarandi F, Ardalan FA, Khanafshar N. Cutaneous metastasis from carcinoma of the cervix at the drain site. *Gynecol Oncol* 2002; **85**: 209–211.
10 Yamashita H, Nakagawa K, Shiraishi K *et al.* External beam radiotherapy to treat intra- and extra-hepatic dissemination of hepatocellular carcinoma after radiofrequency thermal ablation. *J Gastroenterol Hepatol* 2006; **21**: 1555–1560.

© 2009 Japanese Dermatological Association

THE JOURNAL OF GENE MEDICINE
J Gene Med 2009; 11: 598–604.
Published online 27 April 2009 in Wiley InterScience (www.interscience.wiley.com) DOI: 10.1002/jgm.1337

RESEARCH ARTICLE

Enhanced transgene expression in the mouse skeletal muscle infected by the adeno-associated viral vector with the human elongation factor 1α promoter and a human chromatin insulator

Mayuyo Mori-Uchino[1,2†]
Takamasa Takeuchi[1†]
Isao Murakami[1,3]
Tetsu Yano[2]
Toshiharu Yasugi[2]
Yuji Taketani[2]
Keiichi Nakagawa[4]
Tadahito Kanda[1]*

[1]*Center for Pathogen Genomics, National Institute of Infectious Diseases, Tokyo, Japan*

[2]*Department of Obstetrics and Gynecology, Faculty of Medicine, The University of Tokyo, Tokyo, Japan*

[3]*Department of Obstetrics and Gynecology, School of Medicine, Keio University, Tokyo, Japan*

[4]*Department of Radiology, Graduate School of Medicine, The University of Tokyo, Tokyo, Japan*

*Correspondence to:
Tadahito Kanda, Center for Pathogen Genomics, National Institute of Infectious Diseases, 1-23-1 Toyama, Shinjuku-ku, Tokyo 162-8640, Japan.
E-mail: kanda@nih.go.jp

†Both investigators contributed equally and should be considered as senior authors.

Received: 11 September 2008
Revised: 26 January 2009
Accepted: 18 March 2009

Copyright © 2009 John Wiley & Sons, Ltd.

Abstract

Background Efficient and continuous expression of a therapeutic transgene is a key factor for improving the efficacy of gene therapy. Some insulators are known to contribute to continuous high-level expression of a therapeutic transgene.

Methods Using the human AAVS1 insulator (DHS) found in the AAVS1 DNase I hypersensitive site, chicken β-globin insulator (cHS4) and sea urchin arylsufatase insulator (Ars), we newly constructed three recombinant adeno-associated virus vectors (rAAV) and examined their capability of transducing the mouse quadriceps muscle.

Results DHS increased transgene expression from the human elongation factor 1α promoter (EF) by 1000-fold, up to the high level achieved by the human cytomegalovirus immediate early promoter/enhancer (CMV), which comprises an extremely strong promoter for driving a transgene. cHS4 enhanced the expression by 100-fold, whereas Ars did not. The enhanced expression was maintained for at least 24 weeks. Vector copy numbers were similar with and without DHS or cHS4; thus, the enhancement is most likely due to up-regulated transcription. Neither DHS, nor cHS4 affected transgene expression from CMV. DHS enhanced expression from the human muscle creatine kinase promoter/enhancer by 100-fold in mice, as did DHS from EF.

Conclusions Although DHS was unable to further enhance high expression from the strong viral enhancer/promoter, it enhanced low expression from the human promoters by 100- to 1000-fold. Thus, DHS may be useful for constructing rAAVs that express a therapeutic transgene from less efficient, tissue specific promoters. Copyright © 2009 John Wiley & Sons, Ltd.

Keywords AAV vector; insulator; transduction of muscle

Introduction

Recombinant adeno-associated virus vector (rAAV), which is highly stable and can infect various organs, is considered to be suitable for *in vivo* administration in gene therapy [1,2]. Because the rAAV genome lacks the viral rep gene, whose product mediates the viral DNA replication and the integration of the viral DNA into the AAVS1 region in chromosome 19, the rAAV genome is

not replicable and does not undergo site-specific integration [3,4]. Recent studies have shown that the vast majority of infected rAAV genomes persist in the muscle in an extra-chromosomal circular form [5–7]. A variety of integration junctions between the rAAV genome and host chromosome have been recovered, indicating that a small fraction of the infected rAAV genomes is integrated at random sites [8]. The expression of transgene introduced by rAAV lasts for a long time, and some successful animal data have allowed human clinical trials to be conducted using rAAVs for the treatment of cystic fibrosis, hemophilia B, and Parkinson's disease [9–11].

Efficient and continuous expression of a therapeutic transgene is a key factor for improving the efficacy of gene therapy. Insulators comprise an element with the potential to induce continuous high-level expression of a transgene. Insulators have been shown experimentally to comprise the DNA sequences that define a domain of gene expression by directionally protecting a promoter from enhancers in different domains and by acting as a boundary to the surrounding heterochromatin [12]. Heterochromatinization is associated with silencing epigenetic modifications, including histone deacetylation and DNA methylation. Insulators appear to have mechanisms that counteract the silencing effects of heterochromatin [13,14].

In previous studies, insulators were inserted into vector genomes to protect their transgene expression cassettes from the negative influences brought about by adjacent elements. Expression of the transgene integrated in the host chromosome with a lentivirus vector carrying the chicken β-globin insulator is two-fold higher than that with the insulator-less vector [15]. The chicken β-globin insulator inserted into an adenovirus vector shields a downstream promoter from viral enhancers or silencers that are present in the vector genome [15–18].

In the present study, we constructed rAAVs with the selected insulator and injected them into the skeletal muscle of mice. Because previous studies have indicated that the great majority of rAAV genomes are maintained as extra-chromosomal concatemers, the muscle is an appropriate organ to target when aiming to avoid dilution of vector genomes by host cell division. The insertion of the insulator enhanced transgene expression from the human elongation factor 1α promoter and human muscle creatine kinase promoter/enhancer but did not affect expression from the human cytomegalovirus immediate early promoter/enhancer. These data suggest that the insulator has capacity to enhance transgene expression from a less efficient promoter.

Materials and methods

Vector plasmids

The DNA fragment encoding luciferase, which was excised from pGL4.10 (Promega Corp., Madison, WI, USA) by digestion with *Kpn*I and *Xba*I, was inserted between *Kpn*I and *Xba*I in the multiple cloning site of pEF1/Myc-HisA (Invitrogen Corp., Carlsbad, CA, USA) to yield pEF1α-luc containing a luciferase expression cassette driven by the human elongation factor 1α promoter (EF). pAAV-hrGFP (Stratagene, La Jolla, CA, USA) was digested with *Xho*I and treated by a DNA Blunting Kit (Takara-Bio Inc., Otsu, Japan), followed by further digestion with *Mlu*I, and then electrophoresed on an agarose gel. The DNA fragment containing plasmid backbone, two inverted terminal repeats (ITRs), and hGH-polyA signal (pAAV-ITR) was extracted from the gel. The luciferase expression cassette, which was excised by digestion of pEF1a-luc with *Mlu*I and *Pme*I, was ligated with pAAV-ITR to generate pAAV-EF1-Luc. pAAV-EF1-Luc was digested with *Mlu*I and treated by DNA Blunting Kit, followed by the insertion of *Bam*HI linker to add a *Bam*HI site for the insertion of the insulator fragment. The DHS-S1 region (352 bp, nucleotides 27897527–27897176 of NT_011109.15) [19] was amplified from HeLa genomic DNA by polymerase chain reaction (PCR) with a forward primer having a *Bam*HI site and a reverse primer having a *Bgl*II site, and the resultant fragment was designated as DHS. The chicken β-globin insulator core region (244 bp) [20] and the sea urchin arylsufatase insulator region (578 bp) [21] were generated by annealing of the synthetic complementary oligonucleotides with the sequences of these regions and the recognition sequences of *Bam*HI and *Bgl*II at the 5′ and 3′ ends and the resultant DNA fragments were designated as cHS4 and Ars, respectively. Stuffer, a transcriptionally inert DNA fragment, was amplified from a modified *Renilla* luciferase gene (nucleotides 1329–1679 of phRG-TK (Promega Corp.)) by PCR with a forward primer with a *Bam*HI site and a reverse primer with a *Bgl*II site. Stuffer and the insulator elements were inserted into the *Bam*HI site of pAAV-EF1-Luc to produce pAAV-EF-Stuffer, pAAV-EF-DHS, pAAV-EF-cHS4, and pAAV-EF-Ars, respectively.

A DNA fragment containing the human cytomegalovirus immediate early promoter/enhancer (CMV) and β-globin intron of pAAV-hrGFP was amplified by PCR using primers having *Hin*dIII sites at their 5′ ends. pAAV-EF-Stuffer, pAAV-EF-DHS, pAAV-EF-cHS4, and pAAV-EF-Ars were digested with *Hin*dIII to remove the promoter region (EF) and then ligated with the CMV fragment to produce pAAV-CMV-Stuffer, pAAV-CMV-DHS, pAAV-CMV-cHS4, and pAAV-CMV-Ars, respectively. The C2 site of CMV [22] was removed from pAAV-CMV-Stuffer and pAAV-CMV-DHS to produce pAAV-CMV/E(−)-Stuffer and pAAV-CMV/E(−)-DHS, respectively.

Human muscle creatine kinase enhancer and promoter regions were amplified from human keratinocyte genomic DNA by PCR with the primers for the enhancer (5′-GGATCCTCGAGCCACCCAGGGCCCCGT-3′ and 5′-CTCGAGGGAGGGTCTCGGTCGCCG-3′) and for the promoter (5′-CTCGAGGCCCAGGAAGGGCTGGTGGCTGAA-3′ and 5′-AAGCTTGGCTGGGCTGGGCTGAAGGGG-3′). After cloning the PCR-fragments into pGEM-T easy (Promega Corp.), the enhancer fragment was obtained

Copyright © 2009 John Wiley & Sons, Ltd.

by digestion with *Bam*HI and *Xho*I and the promoter fragment was obtained by digestion with *Xho*I and *Hin*dIII. These two fragments were ligated at *Xho*I site to produce the human muscle creatine kinase promoter/enhancer (CKM) and then ligated with the larger fragment obtained by digestion of pAAV-EF1-Luc with *Bam*HI and *Hin*dIII. Stuffer and the insulator elements were inserted into the *Bam*HI site of the resulting plasmid to produce pAAV-CKM-Stuffer, pAAV-CKM-DHS, pAAV-CKM-cHS4, and pAAV-CKM-Ars, respectively.

Cells

The 293 FT cells were grown in the Dulbecco's modified Eagle's medium (Invitrogen Corp.) containing 10% fetal bovine serum, penicillin (50 μg/ml), kanamycin (100 units/ml) (growth medium) supplemented with G418 (500 μg/ml).

The C2C12 cells [23] were grown in the growth medium and passaged every other day.

rAAVs

The 293 FT cells (5×10^6) were seeded in a 10-cm poly D-lysine dish (BD Biosciences, San Jose, CA, USA) and incubated for 24 h. The cells were transfected with a mixture of a vector plasmid (3 μg) and a helper/packaging plasmid (pEEV-XX2) [24] (9 μg) by using 36 μl of Lipofectamine 2000 (Invitrogen Corp.) per dish. The medium was changed every 24 h with the growth medium supplemented with 1× non-essential amino acid (Invitrogen Corp.) twice. The cells were lysed by freeze–thaw 3 days after the transfection and rAAV was purified by the heparin affinity column method, as described previously [25].

The purified rAAV stock was treated with benzonase for 30 min at 37 °C, followed by overnight treatment of sodium dodecyl sulfate and proteinase K. Vector genome was then extracted by phenol/chloroform extraction, chloroform extraction, and ethanol precipitation. The rAAV genome copy number was measured by real-time PCR (7900HT Fast Real-Time PCR System; Applied Biosystems, Foster City, CA, USA) using Power SYBRGreen PCR Master Mix (Applied Biosystems). The PCR primers for the real-time PCR were set in the luciferase coding sequence. The forward primer was 5′-TTGTGTCCGATTCAGTCATGC-3′ (300 nM final concentration) and the reverse primer was 5′-GGTGAACATGCCGAAGCC-3′ (300 nM final concentration).

Assay of luciferase activity of C2C12 cells infected with the rAAV

The C2C12 cells (1×10^4) were seeded in a 96-well plate, incubated for 24 h, and then inoculated with the rAAV (1×10^8 genome copies). The cells were harvested at 72 h after inoculation and lysed with Passive Lysis Buffer (Promega Corp.). Luciferase activity was measured with Mithras LB940 (Berthold Technologies, Bad Wildbad, Germany) using Luciferase Assay Systems (Promega Corp.). The level of luciferase activity was exhibited in relative light units (RLU).

Assay of luciferase activity of mouse muscles injected with the rAAV

Female BALB/c mice (aged 4 weeks) purchased from Nippon SLC (Shizuoka, Japan) were used in accordance with the local institutional guidelines. The animal was anesthetized with diethyl ether and the quadriceps muscle was injected with rAAV suspended in phosphate-buffered saline (PBS) (50 μl). For comparison, some mice received plain PBS in a similar manner. The entire quadriceps muscle was removed, cut into small pieces (approximately 200 mg), and rapidly frozen on dry ice prior to luciferase analysis. The frozen muscle was mixed with passive lysis buffer with the ratio of 300 μl to 100 mg of tissue. The mixture was then homogenized with a Zirconium bead with MM300 (Retsch GmbH, Haan, Germany) at a frequency of 25 Hz for 15 min, and was left at room temperature for 15 min. The total homogenate of each leg was centrifuged at 12 000 r.p.m. (11 000 × g) for 5 min. The supernatant (20 μl) was used for the luciferase activity assay.

Assay of the vector genome copy number in the muscle

The mouse quadriceps muscle was injected with rAAV of 1×10^{10} genome copies. The muscle was isolated at 4 weeks after injection. Total DNA was extracted from the muscle by using Blood & Cell Culture DNA Midi Kit (Qiagen, Valencia, CA, USA) according to the manufacturer's instructions. The amount of the vector genome DNA in the sample was determined by TaqMan PCR. The TaqMan PCR primers and probe were set in the luciferase coding sequence. The forward primer was 5′-TTGTGTCCGATTCAGTCATGC-3′ (300 nM final concentration) and the reverse primer was 5′-GGTGAACATGCCGAAGCC-3′ (300 nM final concentration), and the probe was 5′-FAM-CTTCGGCAACCAGATCATCCCCG-TAMRA-3′ (200 nM final concentration). The TaqMan PCR conditions used were: 95 °C for 10 min, followed by 40 cycles of 95 °C for 15 s and 60 °C for 1 min in a 25-μl reaction volume. The level of vector DNA in the sample (25 ng of total muscle DNA) was estimated by comparison with the standard curve that had been produced using 1×10^1 to 1×10^5 copies of vector plasmid (coefficient of linearity ≥ 0.995). The result obtained was expressed as the rAAV DNA copy number per nucleus, assuming that one nucleus contains 6 pg of genomic DNA.

Copyright © 2009 John Wiley & Sons, Ltd.

Results

Production of rAAVs with the insulator

Figure 1 shows the rAAV vector genomes constructed in the present study. We selected three insulators: DHS that had been found in a DNase I-hypersensitive site in the AAVS1 region, cHS4, and Ars, and inserted one of the insulators upstream of the promoter in the direction to insulate the luciferase expression cassette. AAVS1 on the q arm of human chromosome 19 is the specific target site of AAV2 for the integration of the viral genome. For comparison, Stuffer, an unrelated DNA fragment from the modified *Renilla* luciferase gene, was used in place of an insulator. We used four promoters: EF, CKM, CMV, and an enhancer-less version of CMV [CMV/E(−)], which lacks the enhancer region of CMV.

The rAAV was produced in the 293 FT cells transfected with the vector plasmid and the helper/packaging plasmid expressing the cap and rep genes of AAV2. The sizes of the vector genomes were in the range 3.66–4.60 kb. The rAAV was designated with the promoter and the insulator used for the construction of its vector genome. For example, rAAV having EF and DHS, CMV and cHS4, and CMV/E(−) and Stuffer were designated as rAAV-EF-DHS, rAAV-CMV-cHS4, and rAAV-CMV/E(−) -Stuffer, respectively. With our procedure, the level of each rAAV produced in a 10-cm culture plate was within the range from 3×10^8 to 5×10^8 genome copies, indicating that these insulators did not affect the packaging of the vector genome.

Transduction of mouse C2C12 cells, a myoblast cell line, with the rAAVs

The inserted DHS or cHS4 enhanced the transgene expression from EF in the C2C12 cells, a myoblast cell line derived from a C3H mouse. However, the insulators did not affect the transgene expression from CMV. The rAAV (1×10^8) was inoculated to the C2C12 cells and luciferase activity of the cell lysate was measured at 72 h after inoculation (Figure 2). The luciferase activities induced by rAAV-EF-DHS and rAAV-EF-cHS4 were two- to three-fold higher than those induced by rAAV-EF-Stuffer (Figure 2A). The luciferase activities induced by rAAV-CMV-DHS, rAAV-CMV-cHS4, and rAAV-CMV-Ars were similar to those induced by rAAV-CMV-Stuffer (Figure 2A). The luciferase activity induced by rAAV-CMV/E(−) was extremely low and was enhanced by the insertion of DHS to the level of 1:200 of rAAV-CMV-Stuffer (Figure 2B), indicating that DHS did not compensate the CMV enhancer. Thus, DHS and cHS4 raised the transgene-expression from EF to a level comparable to that induced from CMV, which is one of the most efficient promoter/enhancer systems.

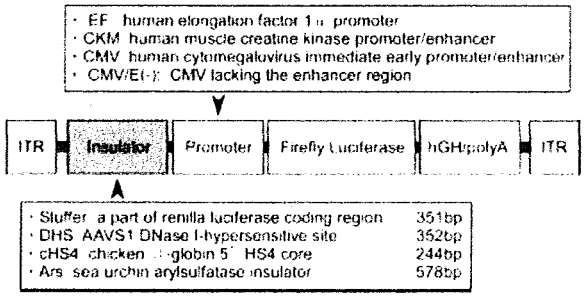

Figure 1. Schematic representation of rAAV genomes. ITR, inverted terminal repeat; hGH/pA, poly A site of human growth hormone gene

Transduction of the mouse muscle with the rAAVs

Figure 3A shows luciferase activities induced by rAAV-EFs in mice. The quadriceps muscle of 4-week-old female BALB/c mice was injected with 50 µl of the rAAV-EFs (1×10^8, 1×10^9 or 1×10^{10} genome copies) in PBS or plain PBS for the measurement of background. Each rAAV preparation was injected into five (in some cases, four or six) legs. The left and right legs were used for different rAAVs to reduce intermouse variability. The luciferase activity of the injected muscle was measured at 4 weeks after injection. Although, at a dose of 1×10^8 genome copies, luciferase activity induced by rAAV-EF-Stuffer was almost at the background level, luciferase activities induced by rAAV-EF-DHS and rAAV-EF-cHS4 were readily detectable. The luciferase levels increased depending on the doses. At all doses tested, the average

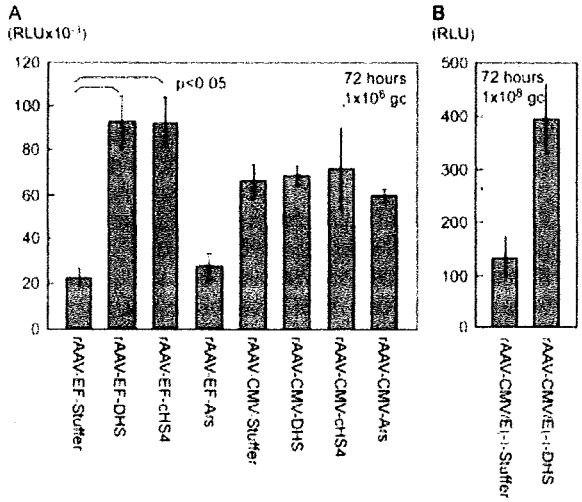

Figure 2. Transduction of C2C12 cells with (A) rAAV-EFs and rAAV-CMVs and (B) rAAV-CMV/E(−)s. C2C12 cells (1×10^4) were inoculated with the indicated rAAV and lysed 72 h later. The luciferase activity of the lysate was measured. The average of three independent experiments is presented with error bars indicating the standard deviation

Copyright © 2009 John Wiley & Sons, Ltd.

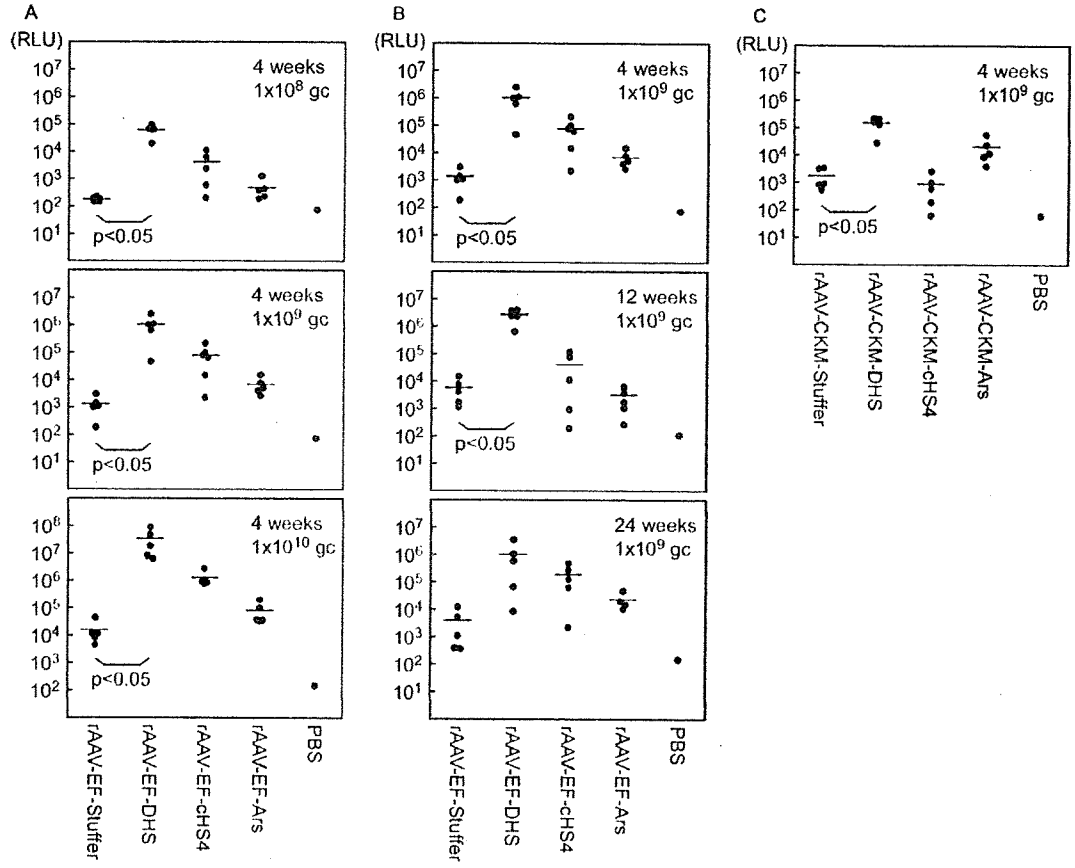

Figure 3. Transduction of the mouse muscle with rAAVs. (A) Levels of luciferase induced by various doses of rAAV-EFs. The mouse quadriceps muscle was inoculated with the indicated rAAV and harvested at 4 weeks after injection. The muscle was minced and lysed, and measured for luciferase activity. Bars indicate the average values. $p < 0.05$ (t-test) was considered statistically significant. (B) Levels of luciferase at 4, 12, and 24 weeks after injection with rAAV-EFs. The mouse quadriceps muscle inoculated with the indicated rAAV was harvested at 4, 12, and 24 weeks after injection. The luciferase activity was measured in a similar manner. Bars indicate the average values. $p < 0.05$ (t-test) was considered statistically significant. (C) Levels of luciferase induced by rAAV-CKMs. The mouse quadriceps muscle inoculated with the indicated rAAV was harvested at 4 weeks after injection. The luciferase activity was measured in a similar manner. Bars indicate the average values. $p < 0.05$ (t-test) was considered statistically significant

luciferase levels induced by rAAV-EF-DHS and rAAV-EF-cHS4 were 1000-fold and 100-fold higher, respectively, than that induced by rAAV-EF-Stuffer.

The luciferase activity of the mouse muscle injected with the rAAV-EFs of 1×10^9 genome copies was measured at 4, 12, and 24 weeks after injection (Figure 3B). The expression of luciferase continued for at least 24 weeks and the levels were maintained.

Figure 3C shows luciferase activities induced by rAAV-CKMs in mice. The mouse muscle was injected with one of rAAV-CKMs (1×10^9 genome copies) and luciferase activity was measured at 4 weeks after injection. The average of luciferase levels induced by rAAV-CKM-DHS was 100-fold higher than that induced by rAAV-CKM-Stuffer, indicating that DHS enhanced the transgene expression from CKM, similar to the expression from EF, in the mouse muscle.

The insulators did not affect transgene expression from CMV in the mouse muscle. The mouse muscle was injected with one of rAAV-CMVs (1×10^9 genome copies) and luciferase activity was measured at 4 weeks after injection. The luciferase level induced by rAAV-CMVs with insulator was similar to that by rAAV-CMV-Stuffer (Figure 4A). Similarly, the insulators did not affect transgene expression in the mouse muscle from the human ubiquitin C promoter, from which luciferase was induced to a level comparable to that from CMV (data not shown).

The luciferase activity of the muscle injected with rAAV-CMV/E(−)-DHS was slightly higher compared to muscle injected with rAAV-CMV/E(−)-Stuffer (Figure 4B).

To examine the transduction of tissues other than the muscle, rAAV-EFs or rAAV-CKMs (1×10^9 genome copies/250 µl of PBS) was injected to each mouse (five mice for each rAAV) through the tail vain. Because the previous study indicated that rAAVs injected through the tail vain are present mainly in the liver and spleen [24], the entire liver and spleen were harvested 4 weeks later and processed as performed for the quadriceps muscle. A low level of luciferase activity was detected only for

Copyright © 2009 John Wiley & Sons, Ltd.

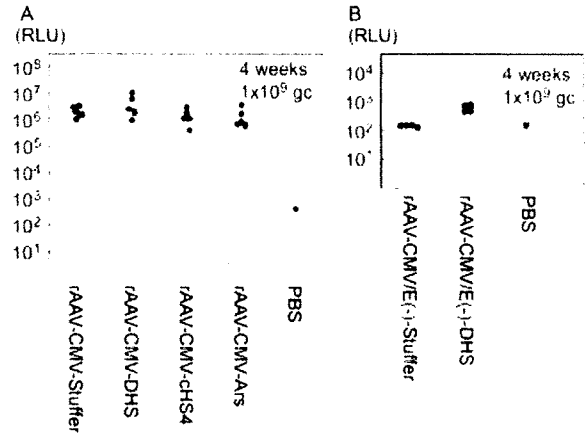

Figure 4. Transduction of the mouse muscle with (A) rAAV-CMVs and (B) rAAV-CMV/E(−) s. The mouse quadriceps muscle was inoculated with the indicated rAAV and harvested at 4 weeks after inoculation. The muscle was minced and lysed, and measured for luciferase activity. Bars indicate the average values

the liver of the mice injected with rAAV-EF-DHS (data not shown), suggesting that rAAV-EF-DHS transduced the liver more efficiently than the other rAAVs did.

Copy number of vector genome in the mouse muscle

The insulators did not affect copy number of the vector genome in the muscle. The rAAV-EFs (1×10^{10} genome copies) were injected to the quadriceps muscle in a similar manner and total DNA was extracted from the muscle at 4 weeks after injection. The level of the vector genome was measured by TaqMan PCR. Table 1 shows the calculated copy number of vector genome per nucleus. There was no significant difference between rAAV-EFs with the insulator and rAAV-EF-Stuffer. The data indicate that the enhanced luciferase activity of the muscle injected with rAAV-EF-DHS or rAAV-EF-cHS4 was not caused by a marked increase in the copy number of vector genome.

Effect of direction and location of DHS on the transduction enhancement

To determine whether or not the direction and location of DHS influence the DHS-mediated transduction enhancement, we constructed rAAV-EF-DHSs having DHS in the opposite direction or downstream of the luciferase gene and examined them for their transduction ability of mouse

Table 1. Copy number of vector genome in the mouse muscle

rAAV injected	Copy number of vector genome/nucleus	Average	SD
rAAV-EF-Stuffer	1.03, 0.76, 0.88, 0.49, 0.58	0.75	0.22
rAAV-EF-DHS	1.00, 1.16, 0.41, 2.65, 0.34	1.11	0.93
rAAV-EF-cHS4	2.39, 1.03, 7.28, 2.42, 0.84	2.79	2.62
rAAV-EF-Ars	1.75, 0.74, 0.87, 0.79, 0.22	0.87	0.55

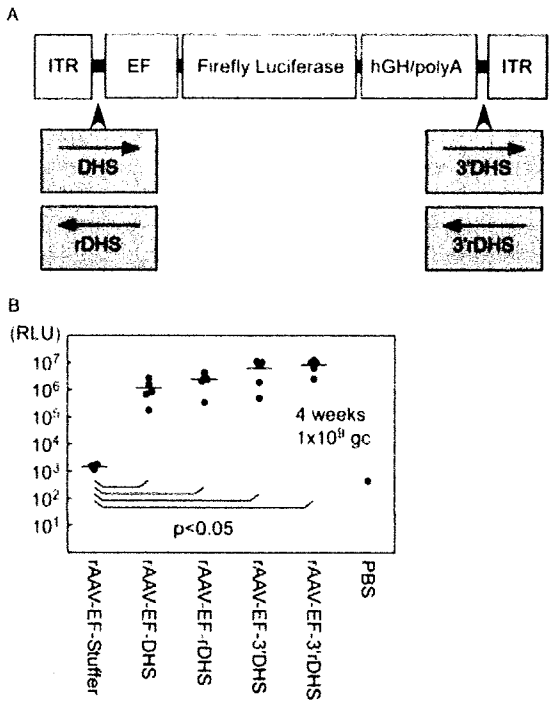

Figure 5. Transduction of the mouse muscle with rAAV-EFs having DHS in the opposite direction and downstream of the transgene. (A) Schematic representation of the various rAAV-EF-DHS genomes. ITR, inverted terminal repeat; rDHS, opposite direction to the transcription of the luciferase gene; hGH/pA, poly A site of human growth hormone gene; 3′DHS and 3′rDHS, DHS inserted downstream of the luciferase gene. (B) Levels of luciferase induced by the rAAV-EFs having DHS in the opposite direction and downstream of the transgene. The mouse quadriceps muscle was inoculated with the indicated rAAV and harvested at 4 weeks after inoculation. The muscle was minced and lysed, and measured for luciferase activity. Bars indicate the average values. $p < 0.05$ (*t*-test) was considered statistically significant

muscle. Figure 5A shows the structure of their vector genomes. The pAAV-EF1-Luc having DHS in the opposite direction was selected to produce rAAV-EF-rDHS. DHS was amplified by PCR with primers with an *Rsr*II site and inserted into the *Rsr*II site (between polyA signal and ITR) of pAAV-EF1-Luc to produce vector genomes for rAAV-EF-3′DHS and rAAV-EF-3′rDHS. These rAAVs were injected to the muscle in a similar manner, and luciferase activity of the muscle was measured 4 weeks later (Figure 5B). The luciferase activities induced by rAAV-EF-rDHS, rAAV-EF-3′DHS, and rAAV-EF-3′rDHS were comparable to that induced by rAAV-EF-DHS, indicating that the DHS-mediated enhancement does not depend on the direction or location of DHS in the AAV vector genome.

Discussion

In the present study, we newly constructed the rAAVs with selected insulators and examined their capability of transducing C2C12 cells and the mouse quadriceps

Copyright © 2009 John Wiley & Sons, Ltd.

muscles. DHS and cHS4 raised the levels of transgene expression from EF by two- to three-fold in C2C12 cells and by 1000- and 100-fold, respectively, in the muscles. DHS also raised the levels of transgene expression from CKM by 100-fold in the muscles. Because the copy numbers of the vector genomes carrying the insulators in the mouse muscles were similar to those of the insulator-less genome, it is likely that the insulators enhanced the transcription from EF and CKM.

DHS did not enhance expression from CMV (one of the most efficient promoter/enhancer found so far) and the human ubiquitin C promoter. The data obtained suggest that DHS did not raise the presumed maximum level of transcription. Most likely, DHS enhances transcription from relatively less efficient promoters, EF and CKM. The transcriptional enhancing function of DHS, a 352 bp fragment, is likely to be useful for rAAV construction with a less efficient tissue specific promoter, such as CKM.

The molecular mechanism of the enhancement is not clear at present. Because previous studies clearly showed that the great majority of rAAV genomes are maintained as extrachromosomal concatemers of circular double-stranded DNA [5–7], DHS and cHS4 likely enhanced transcription of the transgene that was not integrated in cellular DNA. Although, in cellular DNA, the insulator sequences directionally act as boundaries to the surrounding heterochromatin that silences the genes located within [26], those in circular DNA (along with protein factors attached to DNA) may influence the entire chromatin structure of episomes. A possible structural change of the chromatin may account for the findings indicating that the insulator-mediated enhancement was independent of the direction and location of DHS in the AAV vector genome (Figure 5B). DHS inserted into the CMV/E(−) did not compensate the CMV enhancer, suggesting that the enhancing mechanism may be different from that of the classical enhancers. Further studies are required to determine how DHS enhances the transcription from the less efficient promoters.

Acknowledgements

We thank Dr Kunito Yoshiike for critical reading of the manuscript. This work was supported by Health and Labour Sciences Research Grants from the Ministry of Health, Labour and Welfare.

References

1. Flotte TR, Berns KI. Adeno-associated virus: a ubiquitous commensal of mammals. *Hum Gene Ther* 2005; **16**: 401–407.
2. Le Bec C AM. Douar AM. Gene therapy progress and prospects. Vectorology: design and production of expression cassettes in AAV vectors. *Gene Ther* 2006; **13**: 805–813.
3. Weitzman MD, Kyostio SR, Kotin RM, *et al*. Adeno-associated virus (AAV) Rep proteins mediate complex formation between AAV DNA and its integration site in human DNA. *Proc Natl Acad Sci USA* 1994; **91**: 5808–5812.
4. Giraud C, Winocour E, Berns KI. Recombinant junctions formed by site-specific integration of adeno-associated virus into an episome. *J Virol* 1995; **69**: 6917–6924.
5. Duan D, Sharma P, Yang J, *et al*. Circular intermediates of recombinant adeno-associated virus have defined structural characteristics responsible for long-term episomal persistence in muscle tissue. *J Virol* 1998; **72**: 8568–85772.
6. Vincent-Lacaze N, Snyder RO, Gluzman R, *et al*. Structure of adeno-associated virus vector DNA following transduction of the skeletal muscle. *J Virol* 1999; **73**: 1949–55.
7. Schnepp BC, Clark KR, Klemanski DL, *et al*. Genetic fate of recombinant adeno-associated virus vector genomes in muscle. *J Virol* 2003; **77**: 3495–3504.
8. Nakai H, Iwaki Y, Kay MA, *et al*. Isolation of recombinant adeno-associated virus vector-cellular DNA junctions from mouse liver. *J Virol* 1999; **73**: 5438–5447.
9. Flotte T, Carter B, Conrad C, *et al*. A phase I study of an adeno-associated virus-CFTR gene vector in adult CF patients with mild lung disease. *Hum Gene Ther* 1996; **7**: 1145–1159.
10. Kay MA, Manno CS, Ragni MV, *et al*. Evidence for gene transfer and expression of factor IX in haemophilia B patients treated with an AAV vector. *Nat Genet* 2000; **24**: 257–261.
11. Kaplitt MG, Feigin A, Tang C, *et al*. Safety and tolerability of gene therapy with an adeno-associated virus (AAV) borne GAD gene for Parkinson's disease: an open label, phase I trial. *Lancet* 2007; **369**: 2097–2105.
12. Bell AC, West AG, Felsenfeld G. Insulators and boundaries: versatile regulatory elements in the eukaryotic genome. *Science* 2001; **291**: 447–450.
13. Pikaart MJ, Recillas-Targa F, Felsenfeld G. Loss of transcriptional activity of a transgene is accompanied by DNA methylation and histone deacetylation and is prevented by insulators. *Genes Dev* 1998; **12**: 2852–2862.
14. Burgess-Beusse B, Farrell C, Gaszner M, *et al*. The insulation of genes from external enhancers and silencing chromatin. *Proc Natl Acad Sci USA* 2002; **99**(Suppl 4): 16433–16437.
15. Arumugam PI, Scholes J, Perelman N, *et al*. Improved human β-globin expression from self-inactivating lentiviral vectors carrying the chicken hypersensitive site-4 (cHS4) insulator element. *Mol Ther* 2007; **15**: 1863–1871.
16. Ma Y, Ramazani A, Lewis R, *et al*. High-level sustained transgene expression in human embryonic stem cells using lentiviral vectors. *Stem Cells* 2003; **21**: 111–117.
17. Ye X, Liang M, Meng X, *et al*. Insulation from viral transcriptional regulatory elements enables improvement to hepatoma-specific gene expression from adenovirus vectors. *Biochem Biophys Res Commun* 2003; **307**: 759–764.
18. Ramezani A, Hawley TS, Hawley RG. Performance and safety enhanced lentiviral vectors containing the human interferon-β scaffold attachment region and the chicken β-globin insulator. *Blood* 2003; **101**: 4714–4724.
19. Ogata T, Kozuka T, Kanda T. Identification of an insulator in AAVS1, a preferred region for integration of adeno-associated virus DNA. *J Virol* 2003; **77**: 9000–9007.
20. Recillas-Targa F, Pikaart MJ, Burgess-Beusse B, *et al*. Position-effect protection and enhancer blocking by the chicken β-globin insulator are separable activities. *Proc Natl Acad Sci USA* 2002; **99**: 6883–6888.
21. Akasaka K, Nishimura A, Tanaka K, *et al*. Upstream element of the sea urchin arylsulfatase gene serves as an insulator. *Cell Mol Biol* 1999; **45**: 555–565.
22. Boshart M, Weber F, Jahn G, *et al*. A very strong enhancer is located upstream of an immediate early gene of human cytomegalovirus. *Cell* 1985; **41**: 521–530.
23. Yaffe D, Saxel O. Serial passaging and differentiation of myogenic cells isolated from dystrophic mouse muscle. *Nature* 1977; **270**: 725–727.
24. Mori S, Wang L, Takeuchi T, Kanda T. Two novel adeno-associated viruses from cynomolgus monkey: pseudotyping characterization of capsid protein. *Virology* 2004; **330**: 375–383.
25. Auricchio A, Hildinger M, O'Connor E, *et al*. Isolation of highly infectious and pure adeno-associated virus type 2 vectors with a single-step gravity-flow column. *Hum Gene Ther* 2001; **12**: 71–76.
26. Burgess-Beusse B, Farrell C, Gaszner M, *et al*. The insulation of genes from external enhancers and silencing chromatin. *Proc Natl Acad Sci USA* 2002; **99**: 16433–16437.

Copyright © 2009 John Wiley & Sons, Ltd.

Acta Oncol Downloaded from informahealthcare.com by University of Tokyo
For personal use only.

First report on prostate displacements immediately before and after treatment relative to the position during VMAT delivery

KEIICHI NAKAGAWA[1]*, KENSHIRO SHIRAISHI[1]*, SATOSHI KIDA[1], AKIHIRO HAGA[1], KENTARO YAMAMOTO[1], SHIGEKI SAEGUSA[1], ATSURO TERAHARA[1], SAORI ITOH[1], KUNI OHTOMO[1] & KIYOSHI YODA[2]

[1]*Department of Radiology, University of Tokyo Hospital, 7-3-1 Hongo Bunkyo-ku Tokyo 113-8655 Japan and* [2]*Elekta KK, Kobe, Japan*

To the Editor

Previously we reported the first clinical kilovoltage (kV) cone-beam CT (CBCT) imaging during volumetric modulated arc therapy (VMAT) using a linac with an on-board CBCT unit (Elekta Synergy, Crawley, UK) [1], The effect on CBCT image quality during rotational treatments was first presented in ESTRO conference in 2004 [2] and the first clinical in-treatment CBCT images were acquired for rotational lung treatment [3]. The purpose of in-treatment CBCT imaging is direct verification of time-averaged tumor position during treatment. Reported standard deviation of intrafraction prostate movements for 20 patients during 10 fractions was 1.4 mm in cranio-caudal direction [4], which may support the validity of the time-averaged CBCT images. In this letter, prostate displacements immediately before and after treatment relative to the position during VMAT delivery have been reported for the first time. As was described in our previous articles [1,3], the current Synergy system does not allow simultaneous delivery of kV CBCT beams and MV rotational beams. A method for disabling this interlock was therefore investigated and it was deactivated with the first author's responsibility.

A treatment planning system, ERGO++ 1.7.1 (Elekta 3DLine, Milano) was employed to create a VMAT plan for a prostate cancer patient. A single arc consisting of 73 fixed beams was defined with 5 degree spacing. More detailed VMAT delivery and CBCT procedures were described in our previous article [1].

* Equal contributors.

Correspondence: Keiichi Nakagawa, Department of Radiology, University of Tokyo Hospital, 7-3-1 Hongo Bunkyo-ku, Tokyo 113-8655, Japan.

(Received 24 May 2009; accepted 6 June 2009)

RIGHTS
print/ISSN 1651-226X online © 2009 Informa UK Ltd. (Informa Healthcare, Taylor & Francis AS)
341860903101190

Tumor registration was performed between a planning CT image and a CBCT image immediately after patient set-up. CBCT imaging was conducted four times a day once a week for six weeks; the timings were before couch adjustment, after couch adjustment, during VMAT delivery, and immediately after the treatment. The couch adjustment was done by automatic bone matching between planning CT and the CBCT images followed by manual operation based on calcification inside the prostate organ. Subsequently, off-line image registration was performed between two CBCT images of the same day to evaluate prostate displacements using the above mentioned matching procedures.

Figure 1 shows CBCT prostate images of a particular day for a patient with calcification inside the prostate organ. Images in the first row were acquired immediately before VMAT treatment after couch adjustment, the second row refers to images during VMAT delivery, and the third row images were taken immediately after the treatment. Crossing lines indicate the isocenter.

The mean and standard deviation of displacements at the time of pre-treatment against the in-treatment position of all the six days for the patient were 0.1 ± 0.2 mm, -0.3 ± 0.4 mm, and -0.4 ± 0.6mm in lateral, vertical, and longitudinal directions. The mean and standard deviation of displacements at the time of post-treatment against the in-treatment position of all the six days for the same patient were 0.2 ± 0.3 mm, -0.8 ± 0.7 mm, and -0.3 ± 0.6 mm in lateral, vertical, and longitudinal directions. No statistical conclusion can be drawn using the present limited data sets.

In conclusion, displacements of the prostate gland immediately before and after treatment relative to the position during VMAT delivery were reported for the first time using kV CBCT, which may facilitate decision making for subsequent treatment margin or dose adjustment.

Acta Oncol Downloaded from informahealthcare.com by University of Tokyo
For personal use only.

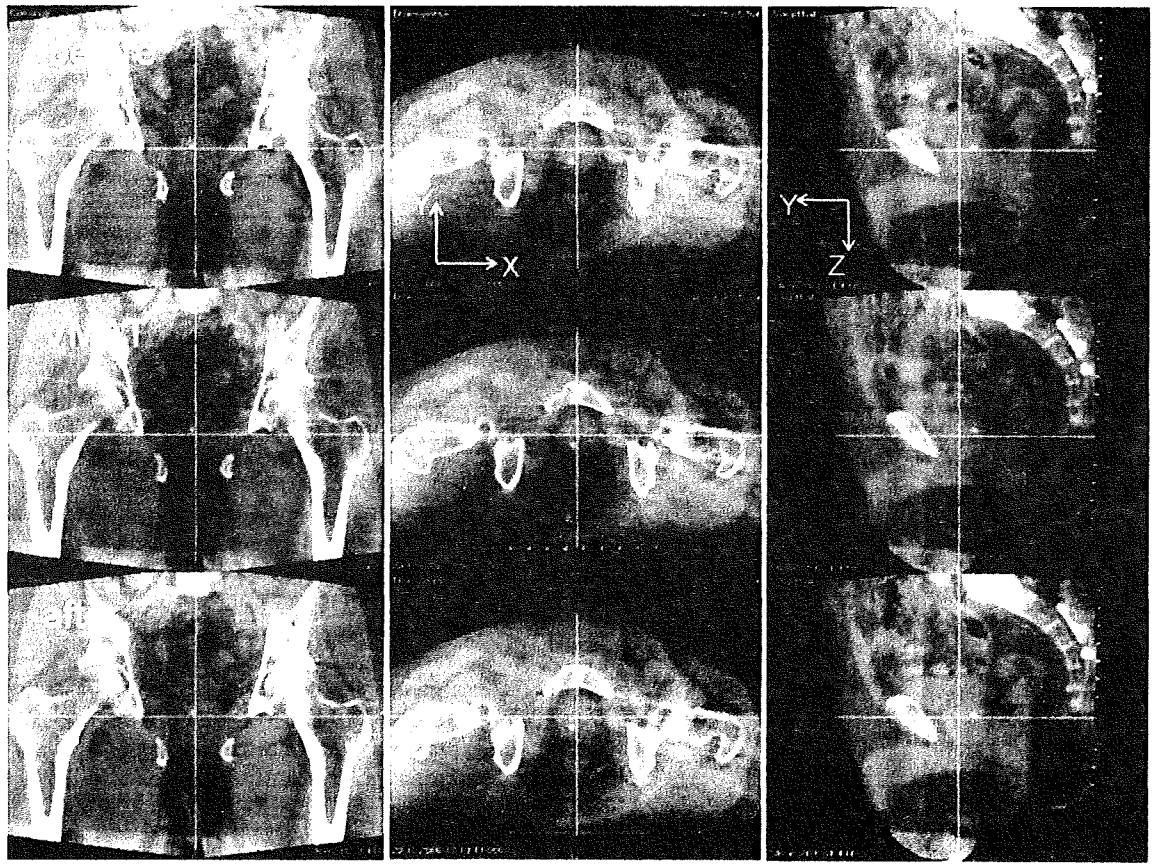

Figure 1. Cone-beam CT images of a prostate cancer patient with calcification inside the prostate organ. Images in the first row were acquired immediately before VMAT treatment after couch adjustment, the second row refers to images during VMAT delivery, and the third row images were taken immediately after the treatment. Crossing lines indicate the isocenter.

RIGHTS

Declaration of interest: Dr. Nakagawa receives research funding from Elekta K.K.

References

[1] Nakagawa K, Haga A, Shiraishi K, Yamashita H, Igaki H, Terahara A, et al. First clinical cone-beam CT imaging during volumetric modulated arc therapy. Radiother Oncol 2009;90: 422–3.

[2] Williams P, Sykes J, Moore CJ. The effects of radiation scatter from simultaneous MV irradiation on kV fluoroscopic and x-ray volume imaging with the Elekta Synergy system, ESTRO, Amsterdam 2004. Radiother Oncol 2004;73 (Suppl 1).

[3] Nakagawa K, Yamashita H, Shiraishi K, Igaki H, Terahara A, Nakamura N, et al. Verification of in-treatment tumor position using kilovoltage cone-beam computed tomography: A preliminary study. Int J Radiat Oncol Biol Phys 2007;69: 970–3.

[4] Haskå TM, Honoré H, Muren LP, Høyer M, Pousen PR. Intrafraction changes of prostate position and geometrical errors studied by continuous electronic portal imaging. Acta Oncol 2008;47:1351–7.

Acta Oncol Downloaded from informahealthcare.com by University of Tokyo
For personal use only.

Acta Oncologica, 2009; 48: 1193–1197

informa
healthcare

ORIGINAL ARTICLE

Quality assurance of volumetric modulated arc therapy using Elekta Synergy

AKIHIRO HAGA[1], KEIICHI NAKAGAWA[1], KENSHIRO SHIRAISHI[1], SAORI ITOH[1], ATSURO TERAHARA[1], HIDEOMI YAMASHITA[1], KUNI OHTOMO[1], SHIGEKI SAEGUSA[1], TOSHIKAZU IMAE[1], KIYOSHI YODA[2] & ROBERTO PELLEGRINI[3]

[1]*Department of Radiology, University of Tokyo Hospital, 7-3-1 Hongo, Bunkyo-ku, Tokyo 113-8655 Japan,* [2]*Elekta KK, Kobe, Japan and* [3]*Elekta, 30 Line, Milano, Italy*

Acta Oncol Downloaded from informahealthcare.com by University of Tokyo
For personal use only.

Abstract

Purpose. Recently, Elekta has supplied volumetric modulated arc therapy (VMAT) in which multi-leaf collimator (MLC) shape, jaw position, collimator angle, and gantry speed vary continuously during gantry rotation. A quality assurance procedure for VMAT delivery is described. *Methods and materials.* A single-arc VMAT plan with 73 control points (CPs) and 5-degree gantry angle spacing for a prostate cancer patient has been created by ERGO++ treatment planning system (TPS), where MLC shapes are given by anatomic relationship between a target and organs at risk and the monitor unit for each CP is optimized based on given dose prescriptions. Actual leaf and jaw positions, gantry angles and dose rates during prostate VMAT delivery were recorded in every 0.25 seconds, and the errors between planned and actual values were evaluated. The dose re-calculation using these recorded data has been performed and compared with the original TPS plan using the gamma index. *Results.* Typical peak errors of gantry angles, leaf positions, and jaw positions were 3 degrees, 0.6 mm, and 1 mm, respectively. The dose distribution obtained by the TPS plan and the recalculated one agreed well under 2%–2 mm gamma index criteria. *Conclusions.* Quality assurance for prostate VMAT delivery has been performed with a satisfied result.

The concept of volumetric modulated arc therapy (VMAT) originated from the conformal avoidance radiation therapy [1] with a dynamical movement of MLC while rotating the gantry. By modulating beam intensity during the gantry rotation, intensity modulated arc therapy (IMAT) was proposed and further investigated [2–6]. VMAT is one of the techniques to realize IMAT by varying gantry speed and dose rate with dynamical movement of MLC and jaw [7]. Recently, this has been clinically available [8–10] and a combination of Elekta Synergy with the latest linac control software and ERGO++ treatment planning system (TPS) is one example.

The purpose of this paper is to investigate how much error is caused in dose distribution due to the fluctuation in the dynamical parameters. The linac controller in Elekta Synergy (Elekta, Crawley, UK), RT Desktop 7.0.1, serves to record measured data of dose rates, gantry angles, MLC and jaw positions with 0.25 s interval during VMAT treatment. We can evaluate the influence of these errors by recalculating the dose distribution with these actual dynamical parameters. Since this is an independent simulation analysis and therefore we may be able to specify the cause when VMAT film verification failed.

Methods and materials

A single-arc VMAT plan for prostate cancer was created by ERGO++ v1.71 TPS (Elekta/3DLine, Milano) with D95 prescription (dose to 95% of target volume) of 76 Gy in 38 fractions. A single arc was discretized into 73 static beams or CPs placed at 5-degree gantry angle intervals between −175 and +175 degrees and the first and last CPs were positioned at −179 and +179 degrees (Figure 1). The field shape for each control point was determined by either conformal or conformal avoidance strategy with a 6 mm leaf margin to Planning Target Volume (PTV). In other words, the rectum was

Correspondence: Akihiro Haga, Department of Radiology, University of Tokyo Hospital, 7-3-1 Hongo, Bunkyo-ku, Tokyo 113-8655 Japan. Tel: +81 3 5800 9002. Fax: +81 3 5800 8786. E-mail: haga-haga@umin.ac.jp

(Received 5 April 2009; accepted 30 May 2009)

RIGHTS

print/ISSN 1651-226X online © 2009 Informa UK Ltd. (Informa Healthcare, Taylor & Francis AS)
341860903081905

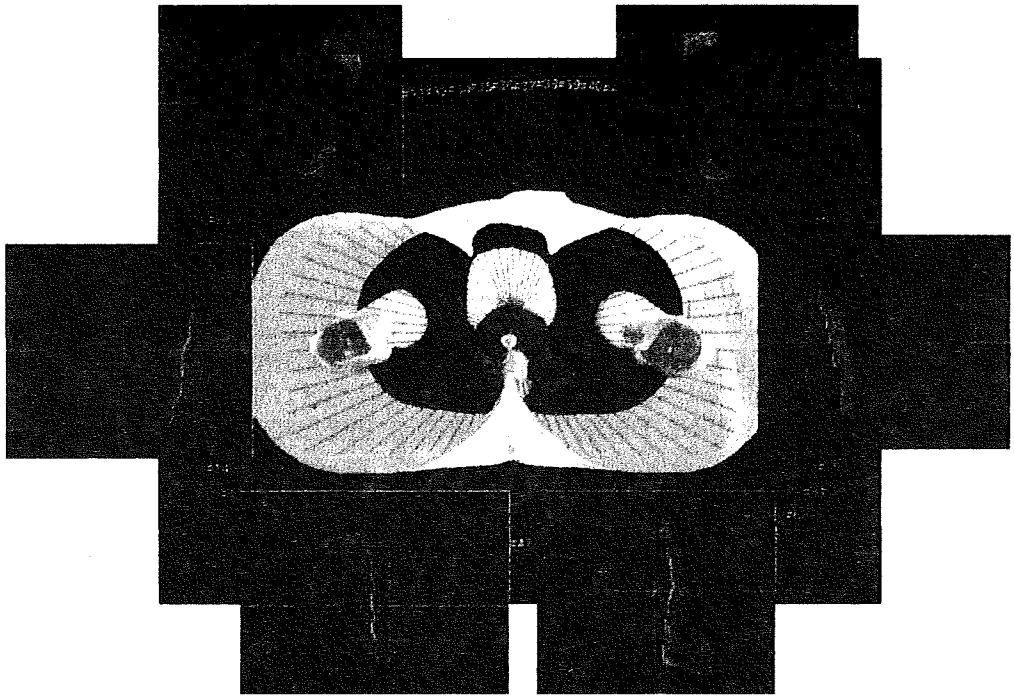

Figure 1. A single-arc VMAT plan with 73 CPs and 5-degree gantry angle spacing for a prostate cancer patient has been created by ERGO++ treatment planning system, where MLC shapes are given by anatomies of target and organs at risk and monitor units for each CP is optimized by simulated annealing algorithm based on given dose prescriptions. The red and pink regions are PTV and rectum, respectively.

Acta Oncol Downloaded from informahealthcare.com by University of Tokyo
For personal use only.

partially shielded by MLC when it was in front of the target in beam's eye view, while the whole target was irradiated when it was in front of the rectum.

In the present study, the collimator angle was fixed at 180 degrees. Beam weights for all CPs were optimized by inverse planning based on the simulated annealing algorithm. Dose grid resolution was 2 mm × 2 mm × 2 mm for 3D calculation. After inverse planning, the CPs were grouped into a single arc with the VMAT sequencer in ERGO++ TPS, where a monitor unit (MU) to be delivered between two adjacent CPs was calculated by adding MUs at the two adjacent CPs and then multiplied by 0.5. The created plan was sent to MOSAIQ v1.6 (Elekta IMPAC, USA), and then delivered by the RT desktop controller.

For dose verification, VMAT plan was transferred to two phantom studies. One was a cylindrical water phantom with 0.015 cc pin-point ionization chamber (Type 31014, PTW, Germany) placed at the isocentre. The other was a pelvic water phantom including a GafChromic film (International Specialty Products, NJ, USA) to measure the dose distribution on axial, coronal, and sagittal planes including the isocentre. The GafChromic film was scanned using a flatbed scanner (EPSON GT-X770, Japan) and the gamma index with 3% of a dose at the measurement point and 3 mm has been evaluated by using DD-system v9.0 (R-tech, Japan).

The linac controller in service mode was capable of recording the actual gantry angle, MLC and jaw positions, and dose rate as a function of time. The MLC and jaw positions in each CP computed by ERGO++ were compared with the corresponding measured values. The cumulative MU error is practically negligible because Elekta VMAT delivery is based on MU-based servo control. Instead, the gantry angle error is discussed, which is defined as the difference between the gantry angle for each CP and the gantry angle where a cumulative MU reaches a specified value. A gantry speed dependence of these errors with the same VMAT plan was also examined by employing two times slower gantry speed than a commonly used clinical speed.

Using the actual data of gantry angle, MLC and jaw positions, and the cumulative MUs, dose distribution was re-calculated using Pinnacle v7.4i TPS (Philips, USA), and the dose in the original plan transferred into Pinnacle was compared with the re-calculated dose distribution.

RIGHTS